Improved photovoltaic efficiency and amplified photocurrent generation in mesoporous n = 1 two-dimensional lead – iodide perovskite solar cells

Febriansyah, Benny; Koh, Teck Ming; Lekina, Yulia; Nur Fadilah Jamaludin; Bruno, Annalisa; Ganguly, Rakesh; Shen, Ze Xiang; Mhaisalkar, Subodh Gautam; England, Jason

2019

Febriansyah, B., Koh, T. M., Lekina, Y., Nur Fadilah Jamaludin, Bruno, A., Ganguly, R., . . . England, J. (2019). Improved photovoltaic efficiency and amplified photocurrent generation in mesoporous n = 1 two-dimensional lead – iodide perovskite solar cells. Chemistry of Materials, 31(3), 890-898. doi:10.1021/acs.chemmater.8b04064

https://hdl.handle.net/10356/142095

https://doi.org/10.1021/acs.chemmater.8b04064

Improved photovoltaic efficiency and amplified photocurrent generation in mesoporous *n* = 1 2D lead-iodide perovskite solar cells

Benny Febriansyah,[†,‡,§] Teck Ming Koh,[†] Yulia Lekina,[||] Nur Fadilah Jamaludin,[†,‡,⊥] Annalisa Bruno,[†] Rakesh Ganguly,[§] Ze Xiang Shen,[||] Subodh G. Mhaisalkar,[†,⊥] and Jason England.[§*]

[†]Energy Research Institute at Nanyang Technological University (ERI@N), Research Techno Plaza, X-Frontier Block Level 5, 50 Nanyang Drive, Singapore 637553, Singapore.

[‡]Interdisciplinary Graduate School (IGS), Nanyang Technological University, 50 Nanyang Avenue, Singapore 639798, Singapore.

[§]Division of Chemistry and Biological Chemistry, School of Physical and Mathematical Sciences, Nanyang Technological University, 21 Nanyang Link, Singapore 637371, Singapore.

[||]Division of Physics and Applied Physics, School of Physical and Mathematical Sciences, Nanyang Technological University, 21 Nanyang Link, Singapore 637371, Singapore.

[⊥]School of Materials Science and Engineering, Nanyang Technological University, 50 Nanyang Avenue, Singapore 639798, Singapore.

ABSTRACT: We utilized two organic dications containing, respectively, a pyridinium and an imidazolium core to construct new *n* = 1 (where *n* refers to the number of contiguous 2D inorganic layers; i.e., not separated by organic cations) two-dimensional (2D) lead-iodide perovskites **1** and **2**. The former material exhibits a (100)- and the latter a very rare 3 × 3 (110)-structural type. Compared with primary ammonium functionality, their constituent ring-centred positive charges have lower charge density. As a result, $[PbI_6]^{4-}$ inter-octahedral distortions of the inorganic lattice are reduced (Pb-I-Pb bond angles are as high as 166° and 174°, respectively). This results in bathochromically shifted optical features. In addition, the compact nature of the dications produce super short lead-iodide sheet separations, with respective iodide-iodide (I···I) distances as small as 4.149 Å and 4.278 Å. These are amongst the shortest separations of adjacent lead-iodide layers, in such materials, ever reported. When crystallized as thin films on top of substrates, the resulting 2D perovskite layers do not adopt a regular growth direction parallel to the surface. Instead, the crystallites grow with no fixed orientation. As a consequence of their proximate inorganic distances and unusual crystallization tendencies, the resulting 2D perovskites exhibit low excitonic activation energies (93.59 meV and 96.53 meV, respectively), enhanced photoconductivity in solar cells, and unprecendented incident photon-to-current conversion rates of up to 60%. More importantly, mesoporous 2D layered perovskite solar cells with power conversion efficiencies (PCEs) of 1.43% and 1.83% were achieved for **1** and **2**, respectively. These are the highest values obtained, thus far, for pure *n* = 1 lead-iodide perovskites and more than 20 times higher than those obtained for materials templated by more conventional cations, such as phenylethylammonium (0.08%).

INTRODUCTION

Two-dimensional (2D) hybrid lead-iodide perovskites with chemical formulas $(RNH_3)_2PbI_4$ or $(NH_3RNH_3)PbI_4$, where R represents an organic functional group,[1-2] are derived from their 3D congeners by slicing the inorganic lattice along certain crystallographic axes (e.g., the (100)- or (110)-planes). This can be induced through incorporation of moderately-sized organic cations, such as the commonly used phenylethylammonium (PEA)[3-4] and 1-butylammonium (BA) ions.[5-6] The resulting 2D materials possess greater synthetic versatility and moisture stability than pure 3D lead-iodide perovskites.[7-8] Thus, attempts have been made to exploit these materials as solar absorbers in photovoltaic (PV) applications.[7-8]

However, the organic cations are known to possess much lower dielectric constants than the neighboring inorganic layers.[9-10] This, combined with constraints imposed by growth of the inorganic lattice in one direction (e.g., parallel to the surface), causes the inorganic layers to experience quantum confinement.[11-12] In addition, the separation of one inorganic layer from the next can be large. For example, in the BA-[13] and PEA-based[3] 2D perovskites the shortest iodide-iodide (I···I) distances are ~8.40 and ~10.20 Å, respectively. As a consequence of these factors, 2D perovskites possess relatively poor semiconducting properties, such as limited interlayer charge transport, large bandgaps, and high excitonic binding energies (e.g. > 300 meV for aliphatic cation-based 2D perovskites).[14-17]

This manifests in typical solar cell and incident photon-to-current efficiencies significantly poorer than their 3D congeners. Thus far, the highest efficiencies reported for devices containing pure 2D lead-iodide perovskite photoactive layers are based upon 1,4-butyldiammonium,[18] histammonium[19] and, very recently, pyrene-O-propyl-ammonium[8] cations. They exhibit respective PCEs of 1.08%, 1.13%, and 1.38%, with typical external quantum efficiencies ranging from 25 to 35%.

One might imagine that the aforementioned optoelectronic issues can be mitigated, and improved photovoltaic characteristics obtained, by judicious selection of ammonium cations. For instance, highly compact dications can engender small lead-iodide sheet separations, which might allow for charge transport enhancement.[18] Additionally, doubly-charged cations exhibit reduced solubility, which leads to rapid crystallization and might result in deviation from typical crystallization behaviour during spin coating.[19] This could be advantageous. Similarly, incorporation of "diffuse" positive charges would be expected to relax the inorganic inter-octahedral tilt angles, thereby resulting in a red shift of the UV-vis absorption profile and a reduced bandgap.[20-21] Lastly, it has been proposed that incorporating an aromatic core might allow for charge transport across the organic layers, thereby reducing electronic confinement.[9]

Spurred by the aforementioned "design criteria", we prepared two new organic dications (Figure 1), designated as pyridinium ethyl ammonium (PyrEA) and imidazolium ethyl ammonium (ImEA), which successfully template formation of the 2D lead-iodide perovskites PyrEA[PbI_4] (**1**) and ImEA[PbI_4] (**2**). In order to disentangle the influence of these cations upon the structural and optoelectronic properties of the resulting materials, the 2D perovskite of the conventional cation phenylethylammonium ($(PEA)_2[PbI_4]$; **3**) is included as a point of comparison. It was selected because PEA-based 2D perovskites have been widely explored for applications, including light emitting diodes (LEDs)[22-23] and field-effect transistors (FETs),[24-25] and in fundamental studies.[26-29]

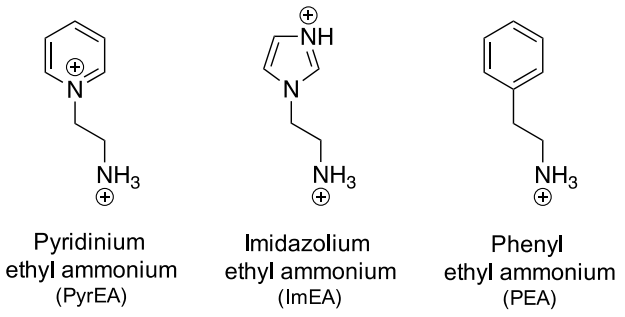

Figure 1. Molecular structures of the dications PyrEA, ImEA, and PEA.

RESULTS AND DISCUSSION

Structural Properties. The crystal structures of **1** and **2** shown in Figures 2a and 2b, respectively, confirm successful formation of 2D lead-iodide perovskites. Despite the structural similarity of PyrEA and ImEA to PEA, the inorganic layer separations in **1** and **2** (9.899 Å and 9.537 Å, respectively) are almost half those in **3** (16.073 Å). This is due to the highly compact nature of the dications PyrEA and ImEA. Significantly, the shortest I···I contacts of 4.278 Å and 4.149 Å in **1** and **2**, respectively, are among the shortest interlayer distances ever recorded for 2D lead-iodide perovskites. For comparison, with histammonium,[19] diimidazolium,[30] 1,4-diammonium naphthalene,[31] and *N,N*-dimethylphenylene-*p*-diammonium[21] cations respective I···I closest contacts of 4.386, 4.423, 4.902, and 4.978 Å are observed.

Interestingly, whereas **1** adopts the more common (100) configuration, the inorganic layer in **2** is corrugated. More specifically, it displays a 3 × 3 (110) structural type. While the first 3 × 3 (110)-oriented lead bromide perovskite was published recently,[32] **2** is the first example in the lead-iodide family templated by a single organic cation. This unusual structure is, presumably, obtained due to the presence and relative position of the N-H functionality within the imidazole core, which controls the hydrogen bonding interactions with neighboring bridging iodide ions of the inorganic layers (2.646 – 3.258 Å, Figure S1). Notably, a similar inorganic architecture was not obtained when the imidazolium-core was replaced with the isomeric pyrazolium-core. Instead, the latter templates formation of a 1D organic-inorganic lead-iodide hybrid, both in bulk materials and thin films (Figure S2). Meanwhile, the related histammonium cation only leads to formation of the conventional (100) structure (Figure S3). A more detailed discussion of the crystal structures of **1**, **2**, and **3** is presented in the SI, with the associated crystallographic and refinement data of all hybrid perovskites crystal structures described herein summarized in Table S1.

Analysis of the crystal structures of **1** and **2** reveals that they have, on the whole, more distorted inorganic lead-iodide octahedra than **3**. The degree of intra-octahedral distortion each perovskite exhibits can be quantified by comparing the following, previously reported, parameters: octahedral elongation (λ_{oct}), octahedral angle variance (σ_{2oct}), and octahedral bond length distortion (Δ_{oct}). The equations for each parameter and an explanation of their meanings can be found in the SI. The resulting values (Table 1) represent the lead-iodide bond length and angle deformations in their constituent $[PbI_6]^{4-}$ octahedra, with larger values indicating a greater degree of distortion.[33-36] The greater distortions in **1** and **2**, relative to **3**, are believed to stem from the comparatively large bulk of their ring-centred positive charges and the associated non-ideal (or absent) hydrogen bonding interactions with iodides of the inorganic layers.

Table 1. Distortion parameters derived from the single crystal X-ray structures of 2D perovskites **1**-**3**[α]

Compound	λ_{oct} (avg)[b]	σ_{2oct} (avg)[c]	Δ_{oct} (avg) ($\times 10^{-4}$)[d]
1	1.0070	24.18	1.24
2	1.0076	23.26	7.97
3	1.0009	2.80	0.61

[α]Averaged distortion parameters are given because X-ray structures of ImEA[PbI_4] and $(PEA)_2[PbI_4]$ contain three and two geometrically distinct octahedra, respectively. Details are given in the SI. [b]Octahedral elongation. [c]Octahedral angle variance. [d]Octahedral bond length distortion.

The effect of structural distortions and ordering of octahedra manifest in single crystal Raman spectroscopy measurements. In order to resolve individual vibrational modes, Raman spectra of **1**-**3** were collected at room temperature (Figure 3) and also at 80 K (Figure S4), where more accurate data fitting can be achieved. Fitting details and parameters are provided in the Supporting Information. It has previously been shown for lead-iodide perovskites that low wavenumber modes are mainly due to vibrations of the inorganic sublattice, while the modes above ~150 cm^{-1} originate from molecular vibrations of the organic cations.[37-39]

According to previous assignments, the modes below ~70 cm^{-1} are associated with I-Pb-I bending. In particular, the two bands around 40 cm^{-1} are likely vibrations distorting the octahedra.[40-42] The presence of two distinct bands is due to inequivalence of the axial and equatorial iodine atoms, as well as distortion of the octahedra.

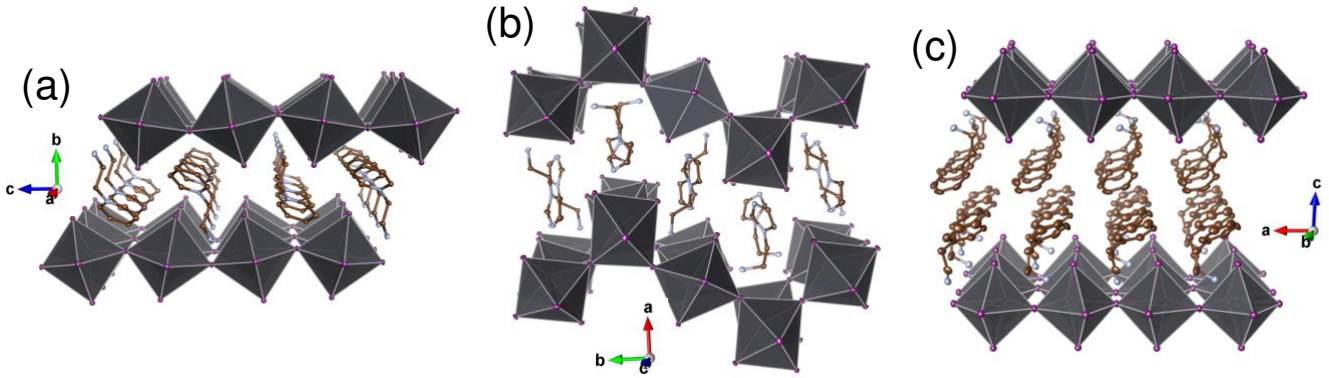

Figure 2. Single crystal X-ray structures of 2D perovskites (a) (PyrEA)[PbI_4] (**1**), (b) (ImEA)[PbI_4] (**2**), and (c) $(PEA)_2[PbI_4]$ (**3**). Inorganic layer separations, defined as the distances between successive mean equatorial planes within an inorganic sheet, are 9.899, 9.537, and 16.073 Å for **1**, **2**, and **3**, respectively. Gray, purple, brown, and blue spheres represent Pb, I, C, and N atoms, respectively. H atoms are omitted for clarity.

Similarly, the vibrations in the range of 70-150 cm^{-1}, assigned to Pb-I stretching,[43] exhibit different frequencies for the in-plane and out-of-plane modes. Most notably, the frequency difference of the two most intense modes in **3** (b_1 and b_2) is equal to 6 cm^{-1}, while in **1** and **2** it reaches 8 and 9 cm^{-1}, respectively. Those two modes can be attributed to distortions of octahedra[42] in different directions, with greater distortion resulting in larger splitting. The bands observed between 90 and 130 cm^{-1} are broader and more poorly resolved in **1** than they are in **3**. This is due to a higher number of distinct vibrational modes in the former relative to the latter, which results from a greater variety of Pb-I bond lengths. Such a scenario is consistent with the more distorted crystal structure of **1** compared to that of **3**.

Meanwhile, the case of **2** is more complicated than those of **1** and **3**. This is most likely due to the distinct 3×3 (110) structural type seen for **2**, wherein the frequency shifts and band broadening might be due to the different connectivity of the octahedra, in addition to the afore discussed structural distortions. It should be emphasized that a better understanding of how the vibrational properties of **1**-**3** depend upon their structural distortions would require precise assignment of their Raman spectra via computational studies.

Optical Properties. Investigation of the photophysical properties of **1**-**3** were undertaken using thin film samples (see SI for experimental details and photos of spincoated thin films of **1**-**3**), as they more closely mimic the PV device settings required for application. To ensure surface consistency, scanning electron microscope (SEM) images were recorded and confirm that all films are smooth and compact (Figure S5). Absorption spectra of all hybrid perovskites under study are presented in Figure 4a and their absorption profiles are summarized in Table 2.

In analogy to other 2D perovskites, the intense bands in the spectra of **1** and **2** at 544 and 522 nm, respectively, can be attributed to excitonic absorptions of the 2D lead-iodide lattices. Both are red shifted with respect to the analogous transition in **3** (514 nm). However, a fair comparison can only reasonably be made between **1** and **3**, since they are both (100)-oriented (and **2** is not). As such, **1** represents a rare example of a heavily bathochromically shifted 2D perovskite, and we are aware of only six other compounds reported to exhibit similarly shifted absorption features.[21, 44-46] It is also noteworthy that **2** has a lower energy excitonic transition than **3**. This is because other works report that (110)-oriented structures characteristically display blue-shifted bandgaps relative to their (100) congeners.[32, 43]

We attribute the aforementioned bathochromic shifts to higher overall Pb-I-Pb bond angles between the adjoining $[PbI_6]^{4-}$ octahedra in **1** (159° to 174°) and **2** (146° to 166°) relative to **3** (151° to 153°) (see Figure S6). This is consistent with previous reports, in which it was revealed through Hückel tight-binding band structure calculations, that combinations of in-plane and out-of-plane distortion angles (Figures S6d and S6e) have the greatest impact on

the tuning of the bandgap. More specifically, more ideal Pb-I-Pb angles were shown to allow for increased orbital overlap, which results in greater band dispersion and, thus, smaller bandgaps.[20, 47-49] We believe that the observed Pb-I-Pb bond angle relaxation is due to the lower charge density of pyridinium and imidazolium cations relative to primary ammonium groups. As a consequence, there is a significantly reduced coulombic driving force for bringing the lead-iodide octahedra into close proximity with the organic countercations, which would otherwise necessitate compression of the Pb-I-Pb bond angles between neighboring octahedra (thus, creating distortion).[20] As such, this work demonstrates that reduction of bond angle distortions can be achieved by judicious choice of organic countercations.

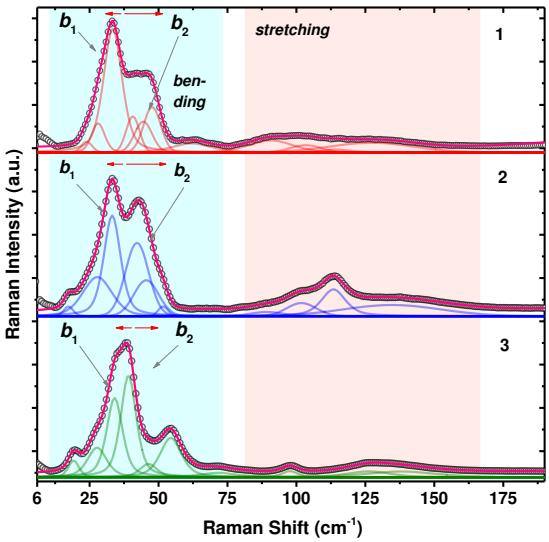

Figure 3. Low wavenumber Raman spectra of (PyrEA)PbI_4 (**1**), (ImEA)PbI_4 (**2**), and $(PEA)_2PbI_4$ (**3**), recorded at room temperature. Circles represent experimental data; red, blue, and green lines are the respective fitting components; and pink lines correspond to the resulting cumulative fits. Spectra are normalised and labels b_1 and b_2 correspond to the most intense vibrational modes.

Table 2. Summary of selected optical parameters for **1**-**3**[α]

Compound	Excitonic absorption (nm)	Bandgap (eV)	Excitonic emission (nm)	RT PL FWHM
1	544	2.48	558	44 nm
2	522	2.54	527	31 nm
3	514	2.58	525	21 nm

[α]Bandgaps are obtained through linear fitting of the thin-film UV-vis absorption spectra (see SI). Excitonic emission position and photoluminescence full width at half-maximum (PL FWHM) are taken from the actual room temperature PL spectra of the 2D perovskites, and not the constituent peaks of Gaussian fits of the data.

In order to eliminate the possibility that the red shifted absorption features of **1** and **2** derives from charge transfer between the inorganic and organic components, we synthesized the (100)-oriented 2D piperidinium ethylammonium perovskite (PipEA)[PbI_4] (Figure S7). Consistent with observations for **1** and **2**, the resulting perovskite is still red in color (Figure S7c, inset), despite the cation used being aliphatic in nature and, thus, having no low-lying unoccupied molecular orbitals. Therefore, it's bathochromically shifted excitonic band at 541 nm (Figure S7c) can be attributed to the mildly distorted Pb-I-Pb angles in its inorganic lattice (value of 164° to 174°), rather than charge transfer.

At room temperature, upon excitation at 480 nm, both **1** and **2** show broad photoluminescences (PLs) consisting of respective narrow bandgap emissions peaks centred at 557 nm (P1a) and 529 nm (P2a) that overlap with broader, longer wavelength Gaussian-fitted peaks at 582 nm (P1b) and 540 nm (P2b), respectively (Figure 4b; Table 2). In contrast, **3** exhibits a typical narrow band emission (full width at half maximum, FWHM = 21 nm) at 525 nm(P3), with a Stokes shift of just 9 nm, that can be fit by a *single* Gaussian. As with that observed in the lead-iodide perovskite templated by 2,2-(ethylenedioxy)bis(ethylammonium),[43] we attribute the existence of two types of emissions in **1** and **2** to the presence of a larger variety of distinct radiative centers in their highly distorted octahedra.

To evaluate the charge carriers dynamics of the materials, time-resolved (TR) PL spectroscopic measurements were performed for **1**-**3**. For all three compounds, two decay time constants were needed to accurately fit the fluorescence decay profiles (Figure 4c and Table S2), which were recorded at their respective PL wavelength maxima. (The residuals for the fit and the instrument response function can be found in Figure S8). It was found that **1** and **2** (τ_{ave} = ~620(60)

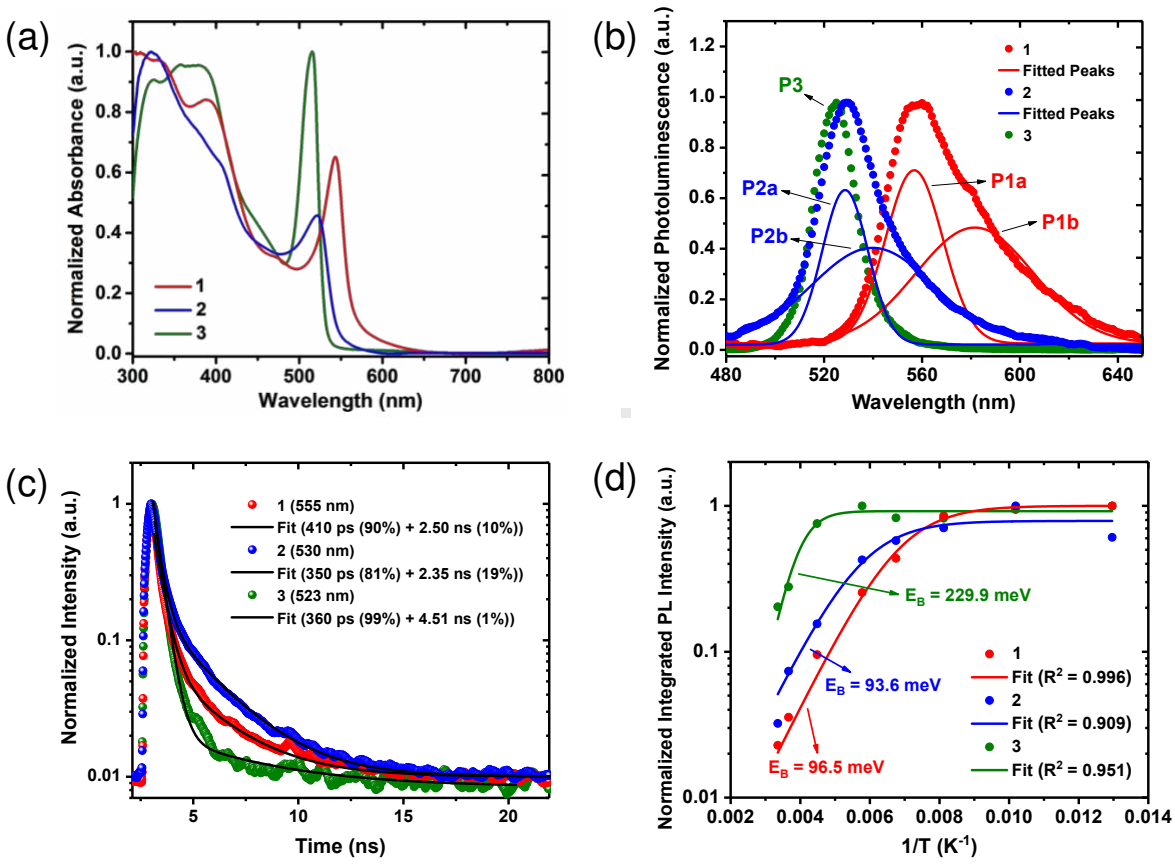

Figure 4. (a) UV-vis absorption spectra of (PyrEA)PbI_4 (**1**), (ImEA)PbI_4 (**2**), and $(PEA)_2PbI_4$ (**3**). (b) Photoluminescence (PL) spectra of **1-3**, plus Gaussian fittings, recorded at RT, using excitation at 405 nm. (c) Time-resolved photoluminescence (TRPL) decays and fits for **1-3**. (d) Temperature-dependent integrated PL intensity for **1-3**. Excitonic binding energies (values given) were extracted by fitting to the Arrhenius equation.

and ~730(70) ps, respectively) feature longer average decay lifetimes than **3** (τ_{ave} = ~400(40) ps). More specifically, **1** and **2** exhibit biexponential decay composed of ~410(40) ps (90%) and ~2.50(0.20) ns (10%) components and ~350(30) ps (81%) and ~2.35(0.20) ns (19%) components, respectively. On the other hand, fitting fluorescene decay of **3** requires ~360(40) ps (99%) and ~4.51(0.40) ns (1%) components. Although it is tempting to attribute these differences to structural factors, further investigations are required before assignment of the decay mechanisms can be made. Regardless, the slower PL decay of **1** and **2**, relative to **3**, which result from greater contributions of the slower decay component, infers that more useful free-charge carriers can be generated in the former two cases during use as solar absorbers.

To further assess the photogenerated charge carriers behavior in **1**, **2** and **3**, we also investigated their emission quenching behavior by carrying out temperature-dependent PL measurements between 77 and 300 K. The resulting spectra are presented in Figure S9. For clarity, intensities of the peak emissions have been normalized. (Figure S10 shows evolution of the PL spectra with retention of relative intensity information.) Satisfactory fitting of the low-temperature PL features of **3** and **1** requires one and two Gaussians, respectively, while three are required for **2**. Details of PL peak deconvolutions are presented in Figure S11. Using P1a, P2a, and P3 extracted from the temperature-dependent measurements, excitonic activation energies of **1**, **2**, and **3** can be estimated by plotting emission intensity against the inverse of temperature (Figure 4d) and fitting them to the following equation:

$$I(T) = \frac{I_0}{1 + Ae^{-E_a/k_BT}} \qquad (1)$$

where, I_0 corresponds to emission intensity at low temperature, E_a to the activation energy, and k_B to the Boltzmann constant.

From the fit of total PL intensity as a function of temperature to Equation 1,[27-28, 53] approximate activation energies of 96.5 and 93.6 meV were extracted for **1** and **2**, respectively. Remarkably, these values are less than half of that obtained for **3**, which in agreement with previous work is estimated to be 229.9 meV.[9] Moreover, the E_a values of **1** and **2** are among the lowest reported for an n = 1 lead-iodide perovskite. We propose that such low values derive from short separation between the inorganic layers, effectively, making them more "3D-like" in character. The activation energy obtained for **3** may well represent the excitonic binding energy and, if that is the case, the decrease of integrated PL intensity upon lowering the temperature can be attributed to partial ionization of the excitons, as was the case in the study conducted in ref [8]. However, this may not be the case for **1** and **2**, as the higher density of defect states arising from their relatively more distorted lead-iodide octahedra could lead to other possibilities. To explore this

possibility, investigations that include single crystal photophysical studies of the materials have been initiated.

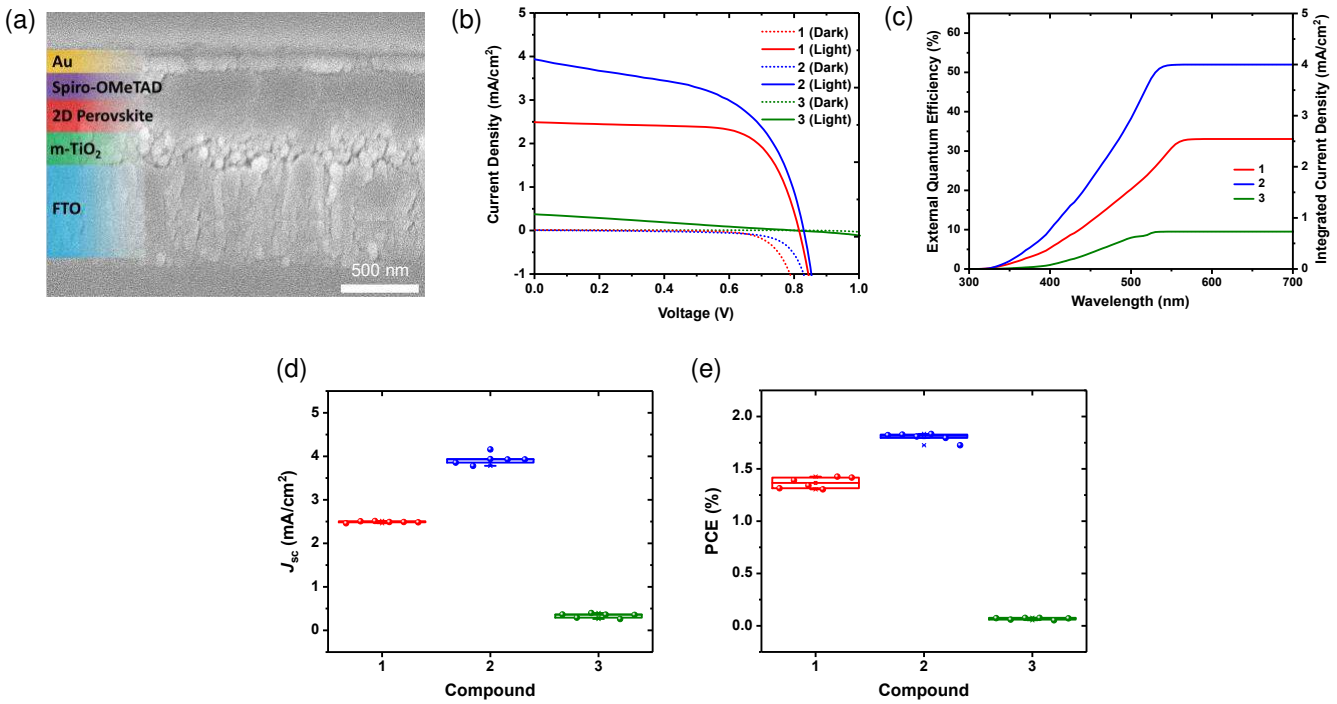

Figure 5. (a) Typical cross-sectional scanning electron micrograph of 2D perovskite solar cells, with mesoporous architecture, employed in this study. (b) Photovoltaic current density-voltage (*J–V*) characteristics of best performing solar cells fabricated using (PyrEA)PbI_4 (**1**), (ImEA)PbI_4 (**2**), and $(PEA)_2PbI_4$ (**3**) as the solar absorbers. Dotted and solid lines represent measurements in the absence and presence of white light irradiation (1 sun; AM 1.5G), respectively. (c) External quantum efficiency (EQE) spectra of the best performing solar cells containing **1-3** (standard, vertical device configuration). Statistical representations of (d) Short-circuit current density (J_{sc}) and (e) power conversion efficiency (PCE) measured for 6 photovoltaic devices each for **1**, **2**, and **3**. Data for the device performance parameters open-circuit voltage (V_{oc}) and fill-factor (FF) are provided in the supporting information.

Application in Solar Cells, Crystallization Behavior, and Electrical Properties. To exploit the superior semiconducting properties of **1** and **2**, (*n* = 1 where *n* refers to number of contiguous inorganic 2D layers; i.e., not separated by organic cations) 2D perovskite solar cells adopting the mesoporous architecture were fabricated (Figure 5a). The band energy diagram specifying the energies of the valence and conduction bands of **1**-**3** relative to the other charge transporting layers comprising the devices is given in Figure S12. The optimized precursor concentration for spin-coating DMF solutions of all materials was found to be 0.50 M. (Details of concentration-dependent device performance parameters, average device performances, and corresponding characterization data can be found in Tables S3-S7.) Current density-voltage *(J-V)* characteristics of the best devices fabricated from each of the 2D perovskites are presented in Figure 5b. To our delight, for active layers of similar thickness, as evidenced by scanning electron micrographs (Figure S13), much higher short circuit current densities (J_{sc}) could be harvested for photovoltaic devices containing **1** and **2** (2.23 and 3.12 mA/cm_2, respectively) compared with those of **3** (0.32 mA/cm_2).

Closer examination revealed that, in addition to reduced inorganic sheet separations, orientation of the 2D perovskite crystallite grains also plays a role in the generation of higher photocurrent in **1** and **2**. Glancing angle X-ray diffraction (GAXRD) patterns for thin films of **1** and **2**, both on top of glass and on top of TiO_2-coated fluorine-doped tin oxide (FTO), show very different behavior to **3** (Figure S14). While **3** prefers to grow with the 2D lead-iodide layers parallel to the substrate, even in device settings (Figure S14c), the crystallites in **1** and **2** tend to display no fixed orientation (Figures S14a and S14b), regardless of the nature of the substrates used. Such a tendency is more pronounced in **1**, where peaks ascribed to (020), (002), (112), (140) and (034) reflections are found to coexist in comparable intensity (see SI). This unique crystallization property is distinct to that of histammonium-based lead-iodide perovskite, where a preferential perpendicular growth orientation was suggested.[19]

The effect of crystallite orientation on photocurrent collection was probed by performing conductivity measurements using a different configuration of electrodes. While the electrodes were placed perpendicular to the perovskite layers in the aforementioned solar cells devices (a "vertical" configuration), in four-probe measurements

they were evaporated parallel to one another (Figure S15a). In the latter setting, upon white light irradiation, **3** displays higher photocurrent. At a bias as low as 2.0 V, the current generated by **3** increases from 14.79 pA (dark) to 63.39 nA (light), corresponding to an on/off ratio of ~4286 (Figure S15d). Meanwhile, induced current only increases from 12.67 pA (dark) to 1.13 nA (light) in the case of **1** and from 10.25 pA (dark) to 0.70 nA (light) for **2**, leading to respective on/off ratios of only 89 and 68 (Figures S15b and S15c). This represents an approximate fifty-fold greater current enhancement in **3** relative to **1** and **2**.

The contrast in conductivity behaviour seen for **1**-**3** between the two device configurations derives from the relative orientations of the electrodes and inorganic lattices. More specifically, when studies are performed for **3** using the four-probe configuration conductivity *within* the lead-iodide layers is measured, while in the perpendicular arrangement of electrodes it is *between* layers. In contrast, regardless of electrode orientation, conductivity in **1** and **2** is always between less-oriented layers. Nonetheless, it is interesting to note that although charge carrier hopping from one less-oriented grain to another in **1** and **2** cannot proceed as efficiently as it does within the lead-iodide layers of **3**, it proves to be more efficient than inter-layer transport, where propagation through space is required for charge collection.

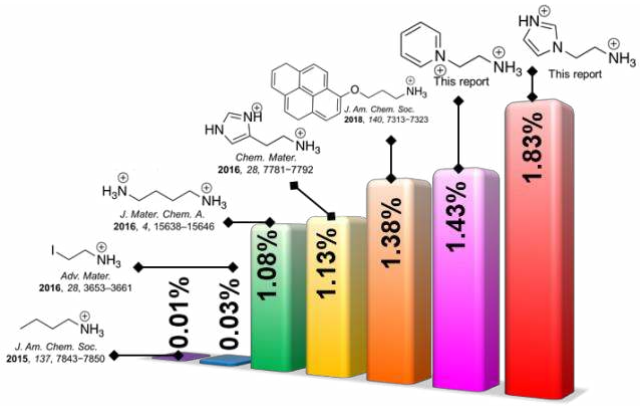

Figure 6. Summary of progress in efficiency of solar cells based upon pure n = 1 2D lead-iodide perovskites as a function of templating organic cations.

Finally, incident photon-to-current efficiency (IPCE) spectra presented in Figure 5c affirm the aforementioned device results. The integrated current densities were found to be 2.49 mA/cm$_2$ and 3.94 mA/cm$_2$ for **1** and **2**, while in the case of **3** it was only 0.73 mA/cm$_2$. In addition, they exhibit absorption onsets similar to their UV-vis absorption spectra, indicating that the bathochromic shifts in **1** and **2** contribute to generation of useful charge carriers. Moreover, the IPCE results also demonstrate better conversion of light to useful charge carriers in **1** and **2**, despite them having similar absorption coefficients as **3** (Figure S16). The superior charge collection properties observed in devices based on **2** relative to those of **1** can be attributed to a number of factors. Not only does the former possess a longer charge carrier lifetime and lower exciton activation energy, it also features better crystallization properties and lower surface roughness. The latter two factors are evident from excitation power-dependent PL experiments (Figure S17), where trap densities of (6.03 ± 1.2) × 10$_{17}$ and (5.68 ± 1.82) × 10$_{17}$ cm$_{-3}$ were measured for **1** and **2**, respectively, and atomic force microscopy (AFM) measurements (Figure S18), from which respective surface roughness values of 43 and 17 nm were obtained.

In particular, the IPCE of up to 60% measured for **2** is, to our knowledge, the best ever demonstrated for a pure n = 1 lead-iodide material. For comparison, histammonium-$_{19}$ and butyl-1,4-diammonium-based$_{18}$ 2D perovskites with comparable inorganic layer separation were previously reported to be capable of demonstrating IPCEs of only 30% and 35%, respectively. The high IPCE values of **1** and **2**, coupled with good open circuit voltages (V_{oc}) of 0.82 – 0.83 V and fill-factors (FF) of over 50 %, allowed photovoltaic cells with power conversion efficiencies (PCEs) of 1.43 – 1.83 % to be obtained for these materials. Statistical representations of J_{sc} and PCE (See Figures S19a and S19b for parameters V_{oc} and FF, respectively) of 6 devices based on **1**, **2**, and **3**, depicted in figures 5d and 5e, confirm reproducibility of the device fabrication process.

The improvement in photovoltaic devices made out of **1** and **2** represents a greater than 20-fold improvement over those fabricated using the well-studied PEA cation (Table 3). More importantly, the best performing cells represent the highest values reported, so far, for n = 1 lead-iodide 2D perovskites. This includes the recent report by Stupp and co-workers detailing enhancement of out-of-plane conductivity of a n = 1 perovskite by use of highly conjugated pyrene organic cations. Their work culminated in a device with a PCE of 1.38%.$_8$ Our distinct approach attests to the advantages of employing compact organic dications, which can engender bathochromatically shifted optical features, very short inorganic layer separation and unique crystallization properties. Figure 6 summarizes the progress in efficiency of solar cells based upon pure 2D lead-iodide perovskites templated by different organic cations.

Table 3. Summary of photovoltaic parameters from the best performing solar cells fabricated from **1-3**$_\alpha$

Compound	V_{oc} (V)	J_{sc} (mA/cm$_2$)	FF (%)	PCE (%)	Thickness (nm)
1	0.82	2.49	70.34	1.43	191 nm
2	0.83	3.94	56.15	1.83	171 nm
3	0.80	0.37	25.17	0.08	183 nm

$_\alpha$Concentration of precursor solution used in spin-coating of all compounds was 0.50 M. V_{oc} = open circuit voltage; J_{sc} = short circuit current density; FF = fill factor; and PCE = power conversion efficiency. Thickness of the active layer was determined from scanning electron micrographs of each sample (see SI for details).

CONCLUSIONS

In conclusion, we have successfully employed pyridinium ethyl ammonium (PyrEA) and imidazolium ethyl ammonium (ImEA) dications to template formation of the new 2D hybrid lead-iodide perovskites (PyrEA)PbI_4 (**1**) and (ImEA)PbI_4 (**2**). Their properties were compared with the well-studied 2D perovskite $(PEA)_2PbI_4$ (**3**), templated by the phenyl ethyl ammonium cation (PEA). As a consequence of the compact nature of their dications, **1** and **2** are endowed with super short 2D inorganic layer separations. Furthermore, the relatively low charge density of the cationic aromatic cores of PyrEA and ImEA leads to relaxation of the Pb-I-Pb inter-octahedral distortions. This causes **1** and **2** to have bathochromically shifted optical features relative to **3**. However, as is apparent from X-ray crystallographic and Raman spectroscopic analyses, the presence of bulky pyridinium and imidazolium rings in **1** and **2**, combined with their inefficient hydrogen bonding interactions with terminal and/or bridging iodides of the inorganic layers, results in an overall increase in structural intra-octahedral distortion compared with **3**. As a consequence, **1** and **2** both exhibit broad photoluminescences at room temperature. Based upon preliminary temperature- and flux density-dependent PL investigations, this can be attributed to the presence of defect states.

Low solubility of the organic dications PyrEA and ImEA, even in polar organic solvents like dimethylformamide (DMF), causes **1** and **2** to manifest unique crystallization behavior. More specifically, upon spincoating, the inorganic layers do not adopt a regular growth direction parallel to the surface of the substrates. Instead, their crystallites have no fixed orientation. Such unusual growth properties facilitate better charge transport and collection within conventional perovskite solar cell (PSC) architectures, in which the electrodes are located on the top and bottom of the devices. This, combined with longer lifetimes of photoinduced charge carriers and lower excitonic activation energies than those of **3**, allows harvest of short-circuit current densities (J_{sc}) from PSCs containing **1** and **2** of more than 2.5mA/cm2. Superior charge collection in these materials is affirmed by incident photons-to-current efficiency (IPCE) measurements for the corresponding devices, which show unprecendented 2D perovskite IPCE conversions of up to 60%. Coupled with good open circuit voltages (V_{oc}) of 0.82 – 0.83 V and fill-factors (FF) of over 50 %, photovoltaic cells with power conversion efficiencies of 1.43 – 1.83 % can be obtained for **1** and **2**. These values are the highest reported, so far, for pure 2D lead-iodide perovskite solar cells.

The current work details a new class of organic dications, wherein close proximity of their positive charges leads to lead-iodide perovskites with significantly enhanced optoelectronic properties. Further work, currently in progress, is directed towards fabrication of photovoltaic devices containing materials composed of mixtures of either PryEA or ImEA with methyl ammonium or formamidinium. This should afford materials with higher numbers of contiguous inorganic layers (i.e., $n > 1$). In addition, more in-depth photophysical investigations of **1** and **2** intended to elucidate the impact of structural distortions upon the optoelectronic properties of 2D lead-iodide perovskites have been initiated.

AUTHOR INFORMATION

Corresponding Author

*E-mail: Jengland@ntu.edu.sg.

Notes

The authors declare no competing financial interest. CIF data for associated crystal structures have been deposited in the Cambridge Crystallographic Data Centre under deposition numbers CCDC 1841680-1841685.

ACKNOWLEDGMENT

The authors would like to acknowledge the funding from the Singapore National Research Foundation through the Singapore–Berkeley Research Initiative for Sustainable Energy (SinBeRISE) CREATE Program, Office of Naval Research Global (ONRG-NICOP-N62909-17-1-2155), and the Competitive Research Program: NRF–CRP14–2014–03. JE thanks NTU for funding (M4081442).

REFERENCES

1. Saparov, B.; Mitzi, D. B. Organic-Inorganic Perovskites: Structural Versatility for Functional Materials Design. *Chem. Rev.* **2016**, *116*, 4558–4596.

2. Cheng, Z.; Lin, J. Layered Organic–Inorganic Hybrid Perovskites: Structure, Optical Properties, Film Preparation, Patterning and Templating Engineering. *Cryst. Eng. Comm.* **2010**, *12*, 2646–2662.

3. Smith, I. C.; Hoke, E. T.; Solis-Ibarra, D.; McGehee, M. D.; Karunadasa, H. I. A Layered Hybrid Perovskite Solar-Cell Absorber with Enhanced Moisture Stability. *Angew. Chem. Int. Ed.* **2014**, *53*, 11232–11235.

4. Quan, L. N.; Yuan, M.; Comin, R.; Voznyy, O.; Beauregard, E. M.; Hoogland, S.; Buin, A.; Kirmani, A. R.; Zhao, K.; Amassian, A.; Kim, D. H.; Sargent, E. H. Ligand-Stabilized Reduced-Dimensionality Perovskites. *J. Am. Chem. Soc.* **2016**, *138*, 2649–2655.

5. Cao, D. H.; Stoumpos, C. C.; Farha, O. K.; Hupp, J. T.; Kanatzidis, M. G. 2D Homologous Perovskites as Light-Absorbing Materials for Solar Cell Applications. *J. Am. Chem. Soc.* **2015**, *137*, 7843–7850.

6. Tsai, H.; Nie, W.; Blancon, J. C.; Stoumpos, C. C.; Asadpour, R.; Harutyunyan, B.; Neukirch, A. J.; Verduzco, R.; Crochet, J. J.; Tretiak, S.; Pedesseau, L.; Even, J.; Alam, M. A.; Gupta, G.; Lou, J.; Ajayan, P. M.; Bedzyk, M. J.; Kanatzidis, M. G. High-Efficiency Two-Dimensional Ruddlesden-Popper Perovskite Solar Cells. *Nature.* **2016**, *536*, 312–316.

7. Koh, T. M.; Thirumal, K.; Soo, H. S.; Mathews, N., Multidimensional Perovskites: A Mixed Cation Approach Towards Ambient Stable and Tunable Perovskite Photovoltaics. *ChemSusChem* **2016**, *9*, 2541–2558.

8. Passarelli, J. V.; Fairfield, D. J.; Sather, N. A.; Hendricks, M. P.; Sai, H.; Stern, C. L.; Stupp, S. I., Enhanced Out-of-Plane Conductivity and Photovoltaic Performance in $n = 1$ Layered Perovskites through Organic Cation Design. *J. Am. Chem. Soc.* **2018,** *140* (23), 7313–7323.

9. Hong, X.; Ishihara, T.; Nurmikko, A. V., Dielectric Confinement Effect on Excitons in PbI_4-based Layered Semiconductors. *Phys. Rev. B.* **1992**, *45*, 6961–6964.

10. Ishihara, T.; Takahashi, J.; Goto, T., Optical Properties Due to Electronic Transitions in Two-Dimensional Semiconductors $(C_nH_{2n+1}NH_3)_2PbI_4$. *Phys. Rev. B* **1990,** *42*, 11099–11107.

11. Ishihara, T., Optical Properties of PbI-based Perovskite Structure. *J. Lumin.* **1994**, *60&61*, 269–274.

12. Tanaka, K.; Kondo, T., Bandgap and Exciton Binding Energies in Lead-Iodide-Based Natural Quantum-Well Crystals. *Sci. Technol. Adv. Mater.* **2016,** *4* (6), 599–604.

13. Stoumpos, C. C.; Cao, D. H.; Clark, D. J.; Young, J.; Rondinelli, J. M.; Jang, J. I.; Hupp, J. T.; Kanatzidis, M. G., Ruddlesden–Popper Hybrid Lead Iodide Perovskite 2D Homologous Semiconductors. *Chem. Mater.* **2016,** *28* (8), 2852–2867.

14. Wu, X.; Trinh, M. T.; Zhu, X. Y., Excitonic Many-Body Interactions in Two-Dimensional Lead Iodide Perovskite Quantum Wells. *J. Phys. Chem. C* **2015,** *119* (26), 14714–14721.

15. Tabuchi, Y.; Asai.; Rikukawa, M.; Sanui, K.; Ishigure, K., Preparation and Characterization of Natural Lower Dimensional Layered Perovskite-Type Compounds. *J. Phys. Chem. Solids* **2000**, *61*, 837–845.

16. Kamminga, M. E.; Fang, H.-H.; Filip, M. R.; Giustino, F.; Baas, J.; Blake, G. R.; Loi, M. A.; Palstra, T. T. M., Confinement Effects in Low-Dimensional Lead Iodide Perovskite Hybrids. *Chem. Mater.* **2016,** *28* (13), 4554–4562.

17. Muljarov, E. A.; Tikhodeev, S. G.; Gippius, N. A.; Ishihara, T., Excitons in Self-Organized Semiconductor/Insulator Superlattices: PbI-Based Perovskite Compounds. *Phys. Rev. B* **1995,** *51* (20), 14370–14378.

18. Safdari, M.; Svensson, P. H.; Hoang, M. T.; Oh, I.; Kloo, L.; Gardner, J. M., Layered 2D Alkyldiammonium Lead Iodide Perovskites: Synthesis, Characterization, and Use in Solar Cells. *J. Mater. Chem. A* **2016,** *4* (40), 15638–15646.

19. Mao, L.; Tsai, H.; Nie, W.; Ma, L.; Im, J.; Stoumpos, C. C.; Malliakas, C. D.; Hao, F.; Wasielewski, M. R.; Mohite, A. D.; Kanatzidis, M. G., Role of Organic Counterion in Lead- and Tin-Based Two-Dimensional Semiconducting Iodide Perovskites and Application in Planar Solar Cells. *Chem. Mater.* **2016,** *28* (21), 7781–7792.

20. Knutson, J. L.; Martin, J. D.; Mitzi, D. B., Tuning the Band Gap in Hybrid Tin Iodide Perovskite Semiconductors Using Structural Templating. *Inorg. Chem.* **2015**, *44*(13), 4699–4705.

21. Hautzinger, M. P.; Dai, J.; Ji, Y.; Fu, Y.; Chen, J.; Guzei, I. A.; Wright, J. C.; Li, Y.; Jin, S., Two-Dimensional Lead Halide Perovskites Templated by a Conjugated Asymmetric Diammonium. *Inorg. Chem.* **2017,** *56* (24), 14991–14998.

22. Era, M.; Morimoto, S.; Tsutsui, T.; Saito, S., Organic-Inorganic Heterostructure Electroluminescent Device Using a Layered Perovskite Semiconductor $(C_6H_5C_2H_4NH_3)_2PbI_4$. *Appl. Phys. Lett.* **1994,** *65* (6), 676–678.

23. Hattori, T.; Taira, T.; Era, M.; Tsutsui, T.; Saito, S., Highly Efficient Electroluminescence from a Heterostructure Device Combined with Emissive Layered-Perovskite and an Electron-Transporting Organic Compound. *Chem. Phys. Lett.* **1996**, *254*, 103–108.

24. Kagan, C. R.; Mitzi, D. B.; Dimitrakopoulos, C. D., Organic-Inorganic Hybrid Materials as Semiconducting Channels in Thin-Film Field-Effect Transistors. *Science* **1999**, *286* (5541), 945–947.

25. Mitzi, D. B.; Dimitrakopoulos, C. D.; Rosner, J.; Medeiros, D. R.; Xu, Z.; Noyan, C., Hybrid Field-Effect Transistor Based on a Low-Temperature Melt-Processed Channel Layer. *Adv. Mater.* **2002**, *14* (23), 1772–1776.

26. Hong, X.; Ishihara, T.; Nurmikko, A. V., Photoconductivity and Electroluminescence in Lead Iodide Based Natural Quantum Well Structures. *Solid State Commun.* **1992**, *84* (6), 657–661.

27. Kitazawa, N.; Aono, M.; Watanabe, Y., Temperature-Dependent Time-Resolved Photoluminescence of $(C_6H_5C_2H_4NH_3)_2PbX_4$ (X=Br and I). *Mater. Chem. Phys.* **2012,** *134* (2-3), 875–880.

28. Gauthron, K.; Lauret, J-S.; Doyennette, L.; Lanty, G.; Al Choueiry, A.; Zhang, S. J.; Brehier, A.; Largeau, L.; Mauguin, O.; Bloch, J.; Deleporte, E., Optical Spectroscopy of Two-Dimensional Layered $(C_6H_5C_2H_4\text{-}NH_3)_2\text{-}PbI_4$ perovskite. *Opt. Express* **2010,** 18 (6), 5912–5919.

29. Shimizu, M.; Fujisawa, J.-I.; Ishi-Hayase, J., Influence of Dielectric Confinement on Excitonic Nonlinearity in Inorganic-Organic Layered Semiconductors. *Phys. Rev. B* **2005,** *71* (20), 205306(1)–205306(9).

30. Tang, Z.; Guan, J.; Guloy, A. M., Synthesis and Crystal Structure of New Organic-Based Layered Perovskites with 2,2′-Biimidazolium Cations. *J. Mater. Chem.* **2001,** *11* (2), 479–482.

31. Lemmerer, A.; Billing, D. G., Lead Halide Inorganic–Organic Hybrids Incorporating Diammonium Cations. *Cryst. Eng. Comm.* **2012,** *14* (6), 1954–1966.

32. Mao, L.; Wu, Y.; Stoumpos, C. C.; Wasielewski, M. R.; Kanatzidis, M. G., White-Light Emission and Structural Distortion in New Corrugated Two-Dimensional Lead Bromide Perovskites. *J. Am. Chem. Soc.* **2017**, *139*(14), 5210–5215.

33. Robinson, K.; Gibbs, G. V.; Ribbe, P. H., A Quantitative Measure of Distortion in Coordination Polyhedra. *Science* **1971**, *172* (3983), 567–570.

34. Thomas, N. W., Crystal Structure-Physical Property Relationships in Perovskites. *Acta Cryst.* **1989**, *B45*, 337–344.

35. Lufaso, M. W.; Woodward, P. M., Jahn-Teller Distortions, Cation Ordering and Octahedral Tilting in Perovskites. *Acta Crystallogr. B* **2004,** *60* (Pt 1), 10–20.

36. Alonso, J. A.; Martinez-Lope, M. J.; Casais, M. T.; Fernandez-Diaz, M. T., Evolution of the Jahn-Teller Distortion of MnO_6 Octahedra in $RMnO_3$ Perovskites (R = Pr, Nd, Dy, Tb, Ho, Er, Y): A Neutron Diffraction Study. *Inorg. Chem.* **2000**, *39* (5), 917–923.

37. Niemann, R. G.; Kontos, A. G.; Palles, D.; Kamitsos, E. I.; Kaltzoglou, A.; Brivio, F.; Falaras, P.; Cameron, P. J., Halogen Effects on Ordering and Bonding of CH_3NH_{3+} in $CH_3NH_3PbX_3$ (X = Cl, Br, I) Hybrid Perovskites: A Vibrational

Spectroscopic Study. *J. Phys. Chem. C* **2016,** *120* (5), 2509–2519.

38. Yin, T.; Fang, Y.; Fan, X.; Zhang, B.; Kuo, J.-L.; White, T. J.; Chow, G. M.; Yan, J.; Shen, Z. X., Hydrogen-Bonding Evolution during the Polymorphic Transformations in $CH_3NH_3PbBr_3$: Experiment and Theory. *Chem. Mater.* **2017,** *29* (14), 5974–5981.

39. Brivio, F.; Frost, J. M.; Skelton, J. M.; Jackson, A. J.; Weber, O. J.; Weller, M. T.; Goñi, A. R.; Leguy, A. M. A.; Barnes, P. R. F.; Walsh, A., Lattice Dynamics and Vibrational Spectra of the Orthorhombic, Tetragonal, and Cubic Phases of Methylammonium Lead Iodide. *Phys. Rev. B* **2015,** *92* (14), 144308(1)–144308(8).

40. Gottesman, R.; Gouda, L.; Kalanoor, B. S.; Haltzi, E.; Tirosh, S.; Rosh-Hodesh, E.; Tischler, Y.; Zaban, A.; Quarti, C.; Mosconi, E.; De Angelis, F., Photoinduced Reversible Structural Transformations in Free-Standing $CH_3NH_3PbI_3$ Perovskite Films. *J. Phys. Chem. Lett.* **2015,** *6* (12), 2332–2338.

41. Ledinsky, M.; Loper, P.; Niesen, B.; Holovsky, J.; Moon, S. J.; Yum, J. H.; De Wolf, S.; Fejfar, A.; Ballif, C., Raman Spectroscopy of Organic-Inorganic Halide Perovskites. *J. Phys. Chem. Lett.* **2015,** *6* (3), 401–406.

42. Leguy, A. M.; Goni, A. R.; Frost, J. M.; Skelton, J.; Brivio, F.; Rodriguez-Martinez, X.; Weber, O. J.; Pallipurath, A.; Alonso, M. I.; Campoy-Quiles, M.; Weller, M. T.; Nelson, J.; Walsh, A.; Barnes, P. R., Dynamic Disorder, Phonon Lifetimes, and the Assignment of Modes to the Vibrational Spectra of Methylammonium Lead Halide Perovskites. *Phys. Chem. Chem. Phys.* **2016,** *18* (39), 27051–27066.

43. Cortecchia, D.; Neutzner, S.; Srimath Kandada, A. R.; Mosconi, E.; Meggiolaro, D.; De Angelis, F.; Soci, C.; Petrozza, A., Broadband Emission in Two-Dimensional Hybrid Perovskites: the Role of Structural Deformation. *J. Am. Chem. Soc.* **2017,** *139* (1), 39–42.

44. Sourisseau, S.; Louvain, N.; Bi, W.; Mercier, N.; Rondeau, D.; Boucher, F.; Buzaré, J.-Y.; Legein, C., Reduced Band Gap Hybrid Perovskites Resulting from Combined Hydrogen and Halogen Bonding at the Organic–Inorganic Interface. *Chem. Mater.* **2007,** *19* (3), 600–607.

45. Mercier, N.; Poiroux, S.; Riou, A.; Batail, P., Unique Hydrogen Bonding Correlating with a Reduced Band Gap and Phase Transition in the Hybrid Perovskites $(HO(CH_2)_2NH_3)_2PbX_4$ (X = I, Br). *Inorg. Chem.* **2004**, *43* (26), 8361–8366.

46. Mao, L.; Ke, W.; Pedesseau, L.; Wu, Y.; Katan, C.; Even, J.; Wasielewski, M. R.; Stoumpos, C. C.; Kanatzidis, M. G., Hybrid Dion-Jacobson 2D Lead Iodide Perovskites. *J. Am. Chem. Soc.* **2018,** *140* (10), 3775–3783.

47. Pradeesh, K.; Nageswara Rao, K.; Vijaya Prakash, G., Synthesis, Structural, Thermal and Optical Studies of Inorganic-Organic Hybrid Semiconductors, R-PbI_4. *J. Appl. Phys.* **2013,** *113* (8), 083523(1)–083523(9).

48. Takahashi, Y.; Obara, R.; Nakagawa, K.; Nakano, M.; Tokita, J-Y.; Inabe, T., Tunable Charge Transport in Soluble Organic–Inorganic Hybrid Semiconductors. *Chem. Mater.* **2007**, *19* (25), 6312–6316.

49. Amat, A.; Mosconi, E.; Ronca, E.; Quarti, C.; Umari, P.; Nazeeruddin, M. K.; Gratzel, M.; De Angelis, F., Cation-Induced Band gap Tuning in Organohalide Perovskites: Interplay of Spin-Orbit Coupling and Octahedra Tilting. *Nano Lett.* **2014,** *14* (6), 3608–3616.

50. Wu, X.; Trinh, M. T.; Niesner, D.; Zhu, H.; Norman, Z.; Owen, J. S.; Yaffe, O.; Kudisch, B. J.; Zhu, X. Y., Trap States in Lead Iodide Perovskites. *J. Am. Chem. Soc.* **2015,** *137* (5), 2089–2096.

51. Mao, L.; Wu, Y.; Stoumpos, C. C.; Traore, B.; Katan, C.; Even, J.; Wasielewski, M. R.; Kanatzidis, M. G., Tunable White-Light Emission in Single-Cation-Templated Three-Layered 2D Perovskites $(CH_3CH_2NH_3)_4Pb_3Br_{10-x}Cl_x$. *J. Am. Chem. Soc.* **2017,** *139* (34), 11956–11963.

52. Neogi, I.; Bruno, A.; Bahulayan, D.; Goh, T. W.; Ghosh, B.; Ganguly, R.; Cortecchia, D.; Sum, T. C.; Soci, C.; Mathews, N.; Mhaisalkar, S. G., Broadband-Emitting 2D Hybrid Organic-Inorganic Perovskite Based on Cyclohexane-bis(methylamonium) Cation. *ChemSusChem* **2017,** *10* (19), 3765–3772.

53. Wu, K.; Bera, A.; Ma, C.; Du, Y.; Yang, Y.; Li, L.; Wu, T., Temperature-Dependent Excitonic Photoluminescence of Hybrid Organometal Halide Perovskite Films. *Phys. Chem. Chem. Phys.* **2014,** *16* (41), 22476–22481.

Authors are required to submit a graphic entry for the Table of Contents (TOC) that, in conjunction with the manuscript title, should give the reader a representative idea of one of the following: A key structure, reaction, equation, concept, or theorem, etc., that is discussed in the manuscript. Consult the journal's Instructions for Authors for TOC graphic specifications.

Insert Table of Contents artwork here